ADVANCED ELECTRONIC MATERIALS Open Access
www.advelectronicmat.de

Analog Signal Rectification and Filtering by a Single Electrolyte-Gated Transistor Based on Reduced Graphene Oxide

Federico Rondelli, Maryam Abouali, Anna De Salvo, Matteo Genitoni, Michele Di Lauro, Luciano Fadiga, and Fabio Biscarini*

Ambipolar materials integrating both p-type and n-type charge transport in Electrolyte-Gated transistors (EGTs) are attractive for simplification of circuit design and power reduction. They are demonstrated as promising candidates for the development of advanced computing systems and sensors. However, the investigation of ambipolar materials for signal processing is still largely unexplored. Among ambipolar materials, reduced graphene oxide (rGO) is shown to be suitable for EGTs, due to its high conductivity (conductivity > 1000 S cm^{-1}) and its processability starting from aqueous graphene oxide dispersions. This work presents ambipolar rGO-EGTs that autonomously perform mathematical operations on oscillatory input signals: phase reversal, full- and half-wave rectification, band-stop and high-pass filtering, according to the operating EGT gate voltage. These results prompt rGO-EGTs as embedded building blocks for in situ real time analog signal processing.

1. Introduction

In living organisms, the[1–5] transmission of electrical and/or chemical signals enables communication between cells, tissues and organs, and plays a crucial role in maintaining homeostasis, regulating growth, facilitating movement, and processing external stimuli.[6]

Recording, processing, and interpretation of biological signals is pivotal when aiming at the investigation of biological systems and at diagnostics, as the detection of altered signals might unveil pathological states. Devices engineered to perform these functions should operate in a bidirectional fashion, interfacing biological systems to collect signals and send them feedback. A breakthrough would be to carry out these bidirectional communications locally and autonomously, opening the way to theranostics operated in an unsupervised closed-loop modality.[7–10]

Organic bioelectronics is an enabling technology toward these goals[11] as its potential in applications from biosensing[12–14] to electrical and electrochemical signal recording in vivo[15–17] was demonstrated. Organic bioelectronic devices rely on organic mixed ionic-electronic conductive (OMIEC) materials whose electronic conductivity is modulated by ion displacement in and out of the materials. The strong ion-pi interactions enable the conversion of ionic currents into electronic ones, thus enabling straightforward interfacing to biological systems.[18–22] Such devices exhibit spiking current output in response to time-pulsed signals, with memory retention both in the short- and in the long-term.[23–25] Such features lead to the development of organic neuromorphic electronics and of architectures capable of signal transduction, processing, and memory, all embedded in a single device unit, or in simple circuits made of a few devices. Organic neuromorphic devices were demonstrated as specific sensors, as signal classifiers, and to perform logic operations in real-time at the hardware level.[26–30]

The most studied organic bioelectronic device is the Electrolyte-Gated Organic Transistor (EGOT), a three-terminal device constituted by two conductive leads - termed source (*S*) and drain (*D*) electrodes - bridged by a (semi-)conductive organic film. A third terminal - the gate (*G*) – controls the electrochemical potential of an electrolyte bath in contact with the channel, which then is capacitively coupled to the gate. To operate EGOTs, two different biases are applied: one (V_{DS}) between S and D is responsible for the current (I_{DS}) flowing in the channel; the other (V_{GS}) between G and S sets the channel conductivity by displacing ions toward/away from the channel. The modulation of channel

F. Rondelli, M. Abouali, A. De Salvo, M. Di Lauro, L. Fadiga, F. Biscarini
Center for Translational Neurophysiology of Speech and Communication
Fondazione Istituto Italiano di Tecnologia (IIT-CTNSC)
via Fossato di Mortara 17/19, Ferrara 44121, Italy
E-mail: michele.dilauro@iit.it
M. Genitoni, L. Fadiga
Sezione di Fisiologia
Dipartimento di Neuroscienze e Riabilitazione
Università di Ferrara
via Fossato di Mortara 17/19, Ferrara 44121, Italy
F. Biscarini
Life Sciences Dept.
Università di Modena e Reggio Emilia
Via Campi 103, Modena 41125, Italy

The ORCID identification number(s) for the author(s) of this article can be found under https://doi.org/10.1002/aelm.202500445

DOI: 10.1002/aelm.202500445

conductivity by the gate makes EGOTs excellent amplifiers of minute changes of electrostatic potential occurring at any device interface, either by displacement or reorganization of ions, or by electrochemical reactions.[23,31–33] EGOT-based transducers of chemical[34,35] and electrophysiological[36,37] signals were also demonstrated in vivo. They were also explored for a broader ensemble of functionalities, making them candidates for multifunctional devices and circuits aimed at performing local signal processing, without relying on off-line data analysis.[28,38,39]

Most of the reported EGOTs are based on unipolar OMIECs. This makes the design of circuitry for logic operations more complicated as it requires channels of both p- and n-type. An example that will be relevant to the present paper is a recently reported rectifier that requires at least two transistors.[40] Graphene-based ambipolar EGTs exhibit large charge carrier mobilities of both electrons and holes, greater flexibility in device design/operation, and conductivities of holes and electrons controlled by the V_{GS} value. These features allow one to design compact circuitry with a smaller amount of electronic devices if compared to unipolar counterparts, else integration of multiple functionality into one device, all desirable features for devising novel autonomous closed-loop architectures.[1,41]

Here we use reduced graphene oxide (rGO), a cost-effective and scalable alternative to pristine graphene.[1] rGO is a versatile material for electronic devices operated in electrolytic environments, including transistors and sensors.[4,5,42,43] We fabricate our rGO channels in EGTs by the direct electrodeposition of graphene oxide in water dispersions.[44]By a suitable post-deposition reduction, we then condition the rGO channel to attain a charge neutrality point close to zero volts.[45,46] These rGO channels can be used in rGO-based electrolyte-gated transistors (rGO-EGTs) with excellent *I–V* characteristics, neuromorphic functionalities and as non-volatile multi-state memory retention.[2,3,44]

The present work delves into the investigation of such rGO-EGTs in response to stereotypical frequency-encoded voltage patterns. Importantly, solid-state transistors based on graphene and on carbon nanotubes were already characterized in terms of signal response for radiofrequency applications in the MHz-GHz frequency range.[41,47,48] This range largely exceeds the range of interest for biological system operation. Instead, our rGO-EGTs are shown to respond in electrolytes at physiological frequencies.[49] Here, for the first time, we demonstrate rGO-EGTs operated as autonomous dynamic filters and rectifiers of signals in physiologically relevant frequency ranges.

2. Results and Discussion

2.1. Quasi-Static *I–V* Characteristics of rGO-EGTs

rGO-EGTs are fabricated via direct electrodeposition of rGO on gold interdigitated electrodes patterned on a quartz substrate, following the procedure of fabrication and conditioning reported recently[44] (**Figure 1a**). Transfer curves related to the conditioning procedure are shown in Figure S1 (Supporting Information). After the conditioning process, the quasi-static electrical characteristics are investigated, and the results are reported in Figure 1b–d.

Figure 1b displays a typical rGO-EGT transfer characteristic (top panel) and the corresponding g_m profile (bottom panel). Transfer characteristics exhibit symmetrical ambipolar channel current (I_{DS}) trend upon V_{GS} sweeping, with a region of dominant hole conduction (p-branch, red solid line) and a region of dominant electron conduction (n-branch, blue solid line). The crossing point between these two regimes, where hole conductivity equals electron conductivity, is the charge-neutrality point voltage, V_{CNP}. Such a figure of merit can be determined via fitting of the rGO-EGTs transfer characteristics.[50] The proposed procedure yields V_{CNP} values close to 0 V, which is a condition of utmost importance if planning to deal with physiological input signals, i.e., with signals consisting of small frequency-encoded oscillations centered ≈0 V. Noteworthy, the device in Figure 1b exhibits negligible counterclockwise hysteresis, with transconductances as high as 390 µS for the p-branch and 340 µS for the n-branch, at $V_{GS} = -0.4$ V and $V_{GS} = 0.4$ V, respectively.

Figure S2 (Supporting Information) reports an example of transfer characteristics fitting, together with a typical "leakage" current, I_{GS}. In particular, the I_{GS} profile shows a markedly capacitive current, three orders of magnitude lower than I_{DS} within the operational $\underline{VGS}$ window and a negligible faradaic activity, due solely to the non-ideality of the Pt electrode.[51–53] Fitting parameters for this device according to the universal EGT fitting model[50] are reported in Table S1 (Supporting Information). Stability of V_{CNP} over more than 400 transfer sweeps (i.e., more than 3 h of continuous operation) is reported in Figure S3 (Supporting Information).

Output characteristics of the rGO-EGT were also investigated. The results are shown in Figure 1c,d, for the p-branch ($V_{GS} < V_{CNP}$) and the n-branch ($V_{GS} > V_{CNP}$), respectively. Output characteristics exhibit V_{GS}-dependent slopes, consistent with the state-of-the-art concerning carbon-based transistors.[54–56]

2.2. Frequency Response

In the following, we investigate the frequency-dependent characteristics of rGO-EGTs in both p- and n-branches, using monochromatic sinusoidal waves of given frequency (*f*) and amplitude (peak-to-peak voltage, V_{pp}) as input signals. The continuous offset underlying such sinusoidal perturbations, termed $V_{GS,Off}$, spans the entire V_{GS} operational window. The connection layout schematics for frequency-dependent characterization are depicted in **Figure 2a**.

Figure 2b shows the device response to 1 Hz sinusoidal V_{GS} wave superimposed to a $V_{GS,Off} = -0.3$ V ($V_{PP} = 0.1$ V), which lies within the p-branch of the device's operation. The corresponding I_{DS} shows an out-of-phase transduction of the input signal. This is coherent with the fact that less negative V_{GS} values lead to lower I_{DS}, and vice versa. Conversely, Figure 2c shows the very same wave superimposed to a $V_{GS,Off} = +0.3$ V (i.e., in the n-branch). In this case, the input signal is transduced in phase, albeit with a lower relative magnitude if compared to Figure 2b, due to the g_m difference between the two branches (see Figure 1b, bottom panel).

The frequency-dependent response of rGO-EGTs was explored with sinusoidal waves of varying frequencies (from 1 to 500 Hz)

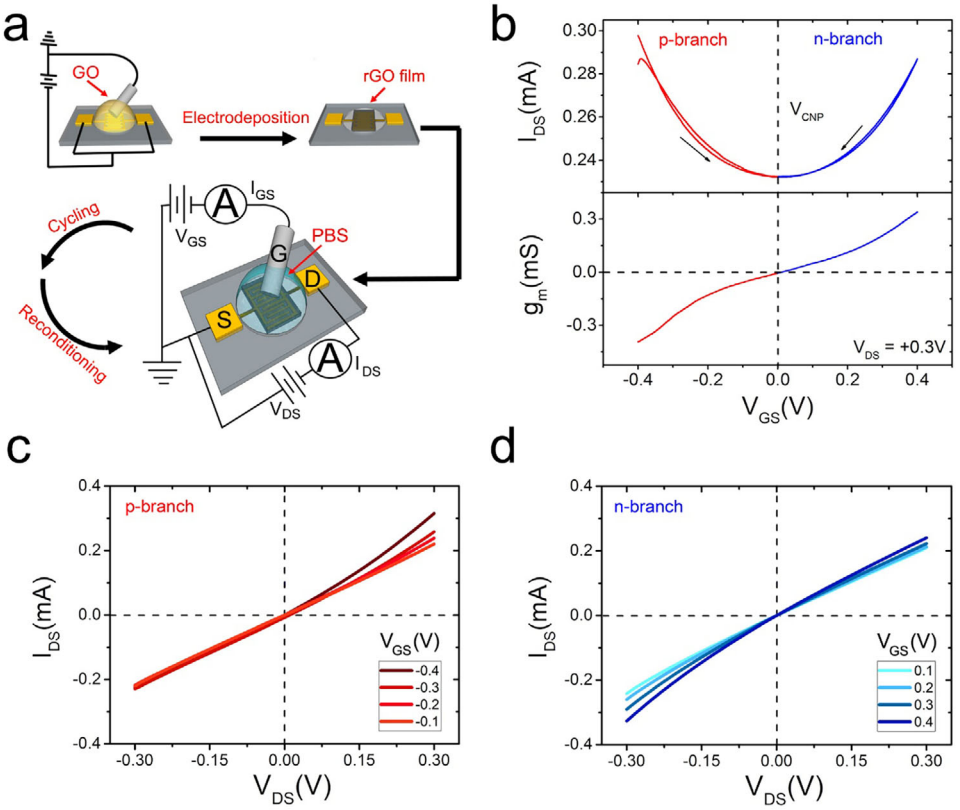

Figure 1. a) Flowchart depicting the procedure of rGO-EGTs fabrication and conditioning, as from Ref. [44]. b) Typical rGO-EGT transfer characteristic (top panel), and the respective g_m profile (bottom panel) obtained by numerical differentiation of I_{DS} with respect to V_{GS}. The color code is used to distinguish between the region of p-conduction (p-branch, red solid line) and the region of n-conduction (n-branch, blue solid line); c) Typical rGO-EGT output characteristics in the p-branch; d) Typical output characteristics in the n-branch.

and V_{pp} values (from 0.2 to 0.013 V), aiming at the evaluation of rGO-EGTs' filtering capability. To provide a quantitative descriptor of frequency-dependent transduction, the (transconductance) parameter γ is introduced, defined as the ratio between I_{DS} peak-to-peak amplitude, $I_{DS,pp}$, and V_{pp} at different f values.

$$\gamma(f) = \frac{I_{DS,pp}}{V_{pp}} \tag{1}$$

For all the investigated sinusoidal waves, the analysis is carried out on segments of V_{GS} and I_{DS} traces, with durations equal to the period $T = 1/f$.

The multivariate dependency of γ upon f and $V_{GS,Off}$ is showcased for both the conduction branches, in Figure 2d,e, for the p- and the n-branch, respectively.

Concerning the p-branch, the Bode plot in Figure 2d exhibits a γ trend resembling the response of a band-stop filter, attenuating signal transduction within a specific frequency range. The frequency of maximum attenuation is termed f_0. The value of f_0 depends on $V_{GS,Off}$, as testified by the shifting of f_0 from 23 Hz at $V_{GS,Off} = -0.15$ V to 103 Hz at $V_{GS,Off} = -0.3$ V.

Such band-stop capability can be further characterized by extracting the cut-off frequencies for $f > f_0$ (we term this cut-off frequency f_H) and $f < f_0$ (we term this cut-off frequency f_L). In particular, f_H exhibits a linear increase on $V_{GS,Off}$ moving from 45 Hz to 256 Hz; differently, f_L remains equal to 1 Hz (i.e., the minimum investigated frequency value) apart from the cases of $V_{GS,Off}$ values lying deep in the p-branch (i.e., for $V_{GS,Off}$ < -0.25 V). The bandwidth (BW) of such band-stop filters, defined as the difference f_H -f_L, can be tuned with $V_{GS,Off}$ to range from 114 to 230 Hz in this experiment. For -0.2 V < $V_{GS,Off}$ < V_{CNP}, rGO-EGTs behave as high-pass filters with a cut-off frequency (f_C) equal to f_H.

For the n-branch, the Bode plot in Figure 2e shows a response typical of high-pass filters, where f_C is only mildly influenced by $V_{GS,Off}$. The dependency of characteristic frequencies of filtering responses on $V_{GS,Off}$ is shown in Figure S4 (Supporting Information).

Frequency dependency of the proposed architecture is also investigated by means of electrochemical impedance spectroscopy in a two-electrode configuration (see Experimental Section). Figure S4 (Supporting Information) summarizes electrochemical impedance spectroscopy results.

The difference between the frequency responses of the two branches can be rationalized by referring to chemo-physical features of the operational electrolyte. In particular, in both cases, the high-pass response is caused by the transition from a capacitor-like to a resistor-like impedance response of the electrolyte, occurring approaching the Maxwell-Wagner relaxation frequency,[57,58] which exhibits a $V_{GS,Off}$ dependency. The

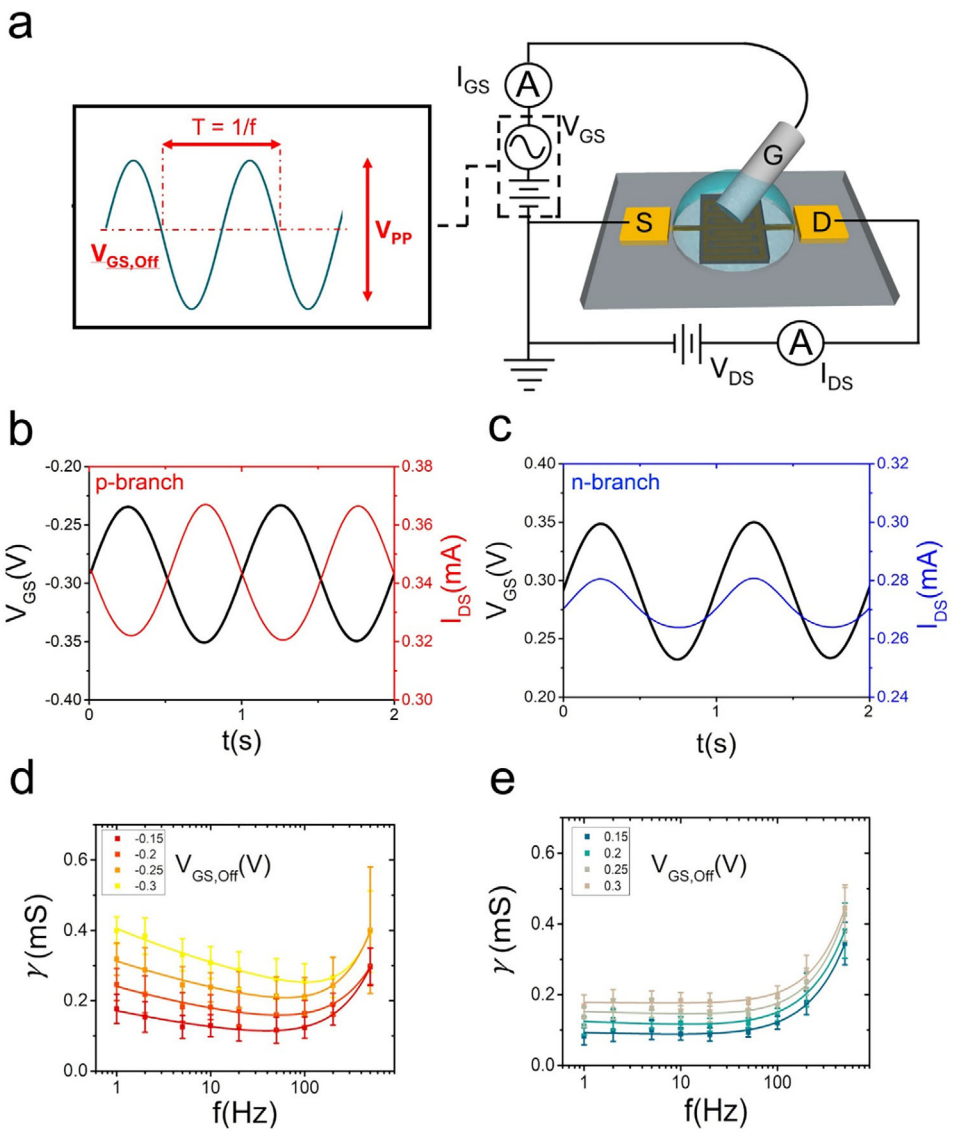

Figure 2. a) Connection layout for frequency-dependent features investigation of rGO-EGTs, highlighting the wavefunction generator connected to the gate terminal and the details of the input sinusoidal voltage wave. The driving voltage (V_{DS}= +0.3 V) is kept constant throughout the measurements. b) Representative trace of administered V_{GS} (black solid line, left axis) and recorded I_{DS} (red solid line, right axis) for $V_{GS,Off}$ = −0.3 V (p-branch). c) Representative trace of administered V_{GS} (black solid line, left axis) and recorded I_{DS} (blue solid line, right axis) for $V_{GS,Off}$ = 0.3 V (n-branch). d) frequency-dependent γ profiles for p-conductive branch at different $V_{GS,Off}$. Markers are averages over 4 devices, with standard errors as error bars. e) frequency-dependent γ profiles for n-conductive branch at different $V_{GS,Off}$. Markers are averages over 4 devices, with standard errors as error bars.

fact that devices operated in their p-branch yield band-stop filters, while behaving only as high-pass filters when operated in the n-branch, can be rationalized in terms of the complex interplay between the asymmetry of p-branch and n-branch transconductances t(already discussed for the comparison between amplitudes of I_{DS} in Figure 2b,c) and the dynamics of the electrolyte, independent on the sign of the majoritary carriers. Regarding the phenomenological band-stop behavior in the p-branch, it is important to stress that it arises from a drop of the p-type transconductance upon frequency increase, while remaining in the resistor-like trait of the impedance spectrum.

If, on the one hand, this does not rule out possible parasitic resonance effects in determining it, on the other hand, it shows a previously unexplored way of technologically exploiting such transconductance drops and parasitic effects, which could be modulated also by acting on the geometry and the composition of the electrolyte.

Interestingly, the grand average of γ values at all frequencies and at all V_{PP} values exhibits a linear trend with $V_{GS,Off}$, with a negative slope for the p-type branch and a positive slope for the n-type one. Importantly, the grand average of γ values at all frequencies and at all $V_{GS,Off}$, does not depend on V_{PP}. All these evidences, reported in Figure S5 (Supporting Information),

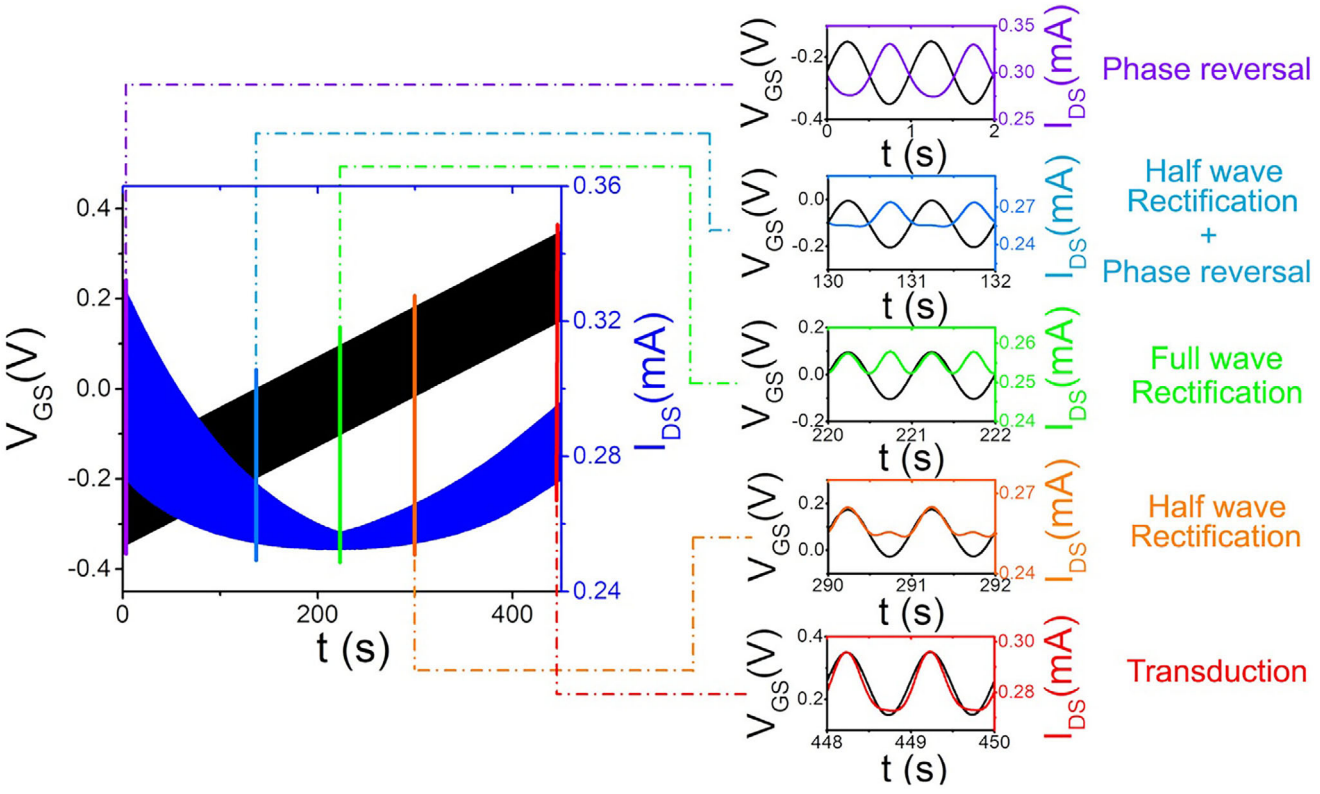

Figure 3. I_{DS} and V_{GS} profiles versus time with insets representing the different operational regions of the rGO-EGT rectifier, highlighting the operation performed on the input signal.

support the claim that γ can be qualitatively regarded as a frequency-dependent transconductance.

2.3. rGO-EGT as a Single-Unit Rectifier

In the previous sections, quasi-static and frequency-dependent characteristics of ambipolar rGO-EGTs were presented, highlighting their tunable filtering capabilities.

This section is focused on the demonstration of a single rGO-EGT for more sophisticated mathematical operations on the input signal, which becomes possible when operating devices in the vicinity of their charge-neutrality point, V_{CNP}.

This experiment is performed using a custom-designed input signal, represented by Equation (2):

$$V_{GS}(t) = \frac{V_{pp}}{2}\sin(2\pi f * t) + \frac{dV_{GS,Off}}{dt} * t + V_{GS,Off,0} \quad (2)$$

Equation (2) represents the input V_{GS} as a function of time (t), resulting from the combination of a sinusoidal wave with frequency f and peak-to-peak amplitude V_{pp}, superimposed to a linear sweep of $V_{GS,Off}$, starting at $V_{GS,Off,0}$ and increasing with a constant rate equal to $dV_{GS,Off}/dt$.

Figure 3 represents the input signal and the corresponding I_{DS} versus time, along with the magnifications of different time windows, corresponding to different operational regimes. Here, f = 1 Hz, $V_{GS,Off,0} = -0.3$ V and $dV_{GS,Off}/dt = 1.3$ mV s^{-1}. As a consequence, the chosen time window of 450 s enables to span the entire V_{GS} range of the transfer characteristics. Interestingly, as the $V_{GS,Off}$ varies from −0.3 to 0.3 V, the amplitude of the sinusoidal I_{DS} response changes, straightforwardly mirroring the device transfer characteristic.

I_{DS} is naturally bound with V_{GS} through the transconductance (g_m). From the numerical definition of g_m as the numerical derivative of I_{DS} with respect to V_{GS} (see Figure 1b), it follows that the p-branch is characterized by a negative g_m. This is, clearly, a mathematical artifact since, in the p-branch, a positive variation of voltage is the hallmark of a less negative voltage, which causes a decrement of the population of the HOMO density of states and, subsequently, a lower p-type current. In the following treatment, both transconductances of the p-type branch ($g_{m,p}$) and of the n-type branch ($g_{m,n}$) are taken as positive quantities, to maintain physical consistency.

The I_{DS} response can be rationalized as:

$$I_{DS}(t) \propto \begin{cases} g_{m,n} * V_{GS}(t) & , if\ V_{GS}(t) > V_{CNP} \\ -g_{m,p} * V_{GS}(t) & , if\ V_{GS}(t) < V_{CNP} \end{cases} \quad (3)$$

Equation (3) can be expanded, including Equation (2):

$$I_{DS}(t) \propto \begin{cases} g_m * \left[\frac{V_{pp}}{2}\sin(2\pi f * t) + \frac{dV_{GS,Off}}{dt} * t + V_{GS,Off,0}\right], if\ V_{GS}(t) > V_{CNP} \\ -g_m * \left[\frac{V_{pp}}{2}\sin(2\pi f * t) + \frac{dV_{GS,Off}}{dt} * t + V_{GS,Off,0}\right], if\ V_{GS}(t) < V_{CNP} \end{cases} \quad (4)$$

As already discussed for Figure 2b,c, when $V_{GS,Off}$ is strongly negative or positive, rGO-EGTs produce a current that retains the

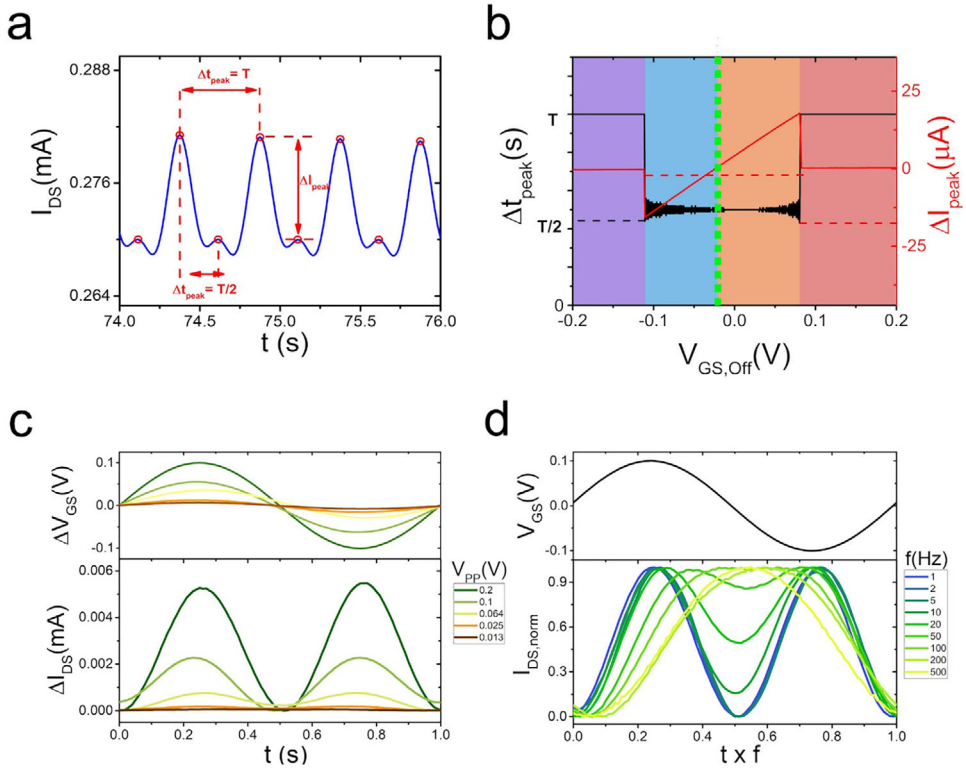

Figure 4. a) Typical I_{DS} trace of half-wave rectification showing Δt_{peak} and ΔI_{peak} determination. b) Rectification profile based on the dependency of Δt_{peak} and ΔI_{peak} on $V_{GS,Off}$, showing the region of rectification in the investigated $V_{GS,Off}$ range. c) Dependency of ΔI_{DS} versus time in the region of perfect rectification at different V_{pp} values. d) Dependency of $I_{DS,norm}$ versus the product of t and f in the full-wave rectification regime at different f values.

sinusoidal behavior of the input signal. This may be regarded as in this regime, the device exhibits full transduction of the V_{GS} sinusoidal component. According to the operational regime, I_{DS} is transduced either in-phase, when $V_{GS,Off}$ lies deeply in the n-branch (red solid line in Figure 3), or out-of-phase when $V_{GS,Off}$ lies deeply in the p-branch (violet solid line in Figure 3). In a signal processing perspective, this endows rGO-EGTs with phase-reversal capability, namely the possibility to select the phase of the transduced signal according to the operator's will. As envisioned by Equation (3), the overall I_{DS} magnitude is set according to the devices' g_m value in the corresponding operational regime.

The peculiar transconductance of ambipolar devices, which shows decreasing trends for both p- and n-branches until reaching its null point at $V_{GS} = V_{CNP}$ (Figure 1), results in the possibility to achieve other desirable signal processing features. Indeed, when the sinusoidal V_{GS} input (black solid line in Figure 3) approaches V_{CNP}, there is a progressively more marked asymmetry of the magnitudes of the currents elicited by the positive and the negative half-cycle of the sinusoidal perturbation, eventually resulting in the complete suppression of one of the two, achieving half-wave rectification. In this case, it is possible to distinguish between two different scenarios:

1) When $V_{GS,Off}$ is mildly negative, the negative sinusoid half cycle is phase reverted, as discussed before, while the positive half cycle falls in a null transconductance region and is hence suppressed (Figure 3, light blue solid line);
2) When $V_{GS,Off}$ is mildly positive, the positive sinusoid half-cycle is fully transduced without phase reversal, and the negative half-cycle is suppressed (Figure 3, orange solid line).

A last scenario is achieved when the input V_{GS} meets the condition $V_{GS,Off} = V_{CNP}$. In this case, both the sinusoidal half-cycles are transduced with equal g_m, albeit the negative half-cycle is phase reverted. This yields a fully rectified I_{DS} current (Figure 3, green solid line). This feature is not commonly reported in single-component electrolyte-gated circuitry, and has been only marginally explored for sensing purposes[5] without discussing its relevance in signal processing applications. Overall, the response in Figure 3 convincingly shows that five different types of wave operations on the channel current can be performed by changing the offset voltage of the rGO-EGT.

As quantitative descriptors of the rectification performances, it is possible to introduce two novel figures of merit on the output signal, namely Δt_{peak} and ΔI_{peak}. A graphical representation of their operational definition is provided in **Figure 4a**.

Δt_{peak} is defined as the time interval between two consecutive positive peaks of the output current. It can be equal to the period (T) of the sinusoidal wave, when the device is operated in non-rectifying regimes, or to its half (T/2) when the device acts as a rectifier. Notice how rectification implies frequency doubling.

ΔI_{peak}, is defined as the difference in I_{DS} magnitude between two consecutive positive peaks. This index is a numerical representation of the already discussed asymmetry of transduction between the two half-waves. In particular, it equals 0 only if

the sinusoidal wave is fully transduced or fully rectified, while it assumes non-zero values in the context of asymmetrical transduction of the input signal.

1) The Δt_{peak} and ΔI_{peak} profiles versus $V_{GS,Off}$, shown in Figure 4b, enable analytical discrimination between the five distinct signal processing "scenarios" discussed in Figure 3:
2) $\Delta t_{peak} = T$, $\Delta I_{peak} = 0$, and $V_{GS,Off} << V_{CNP}$: the rGO-EGT transduces and amplifies the input signal, the output I_{DS} is out-of-phase (violet background region in Figure 4b);
3) $\Delta t_{peak} = T$, $\Delta I_{peak} = 0$, and $V_{GS,Off} >> V_{CNP}$: the rGO-EGT transduces and amplifies the input signal, the output I_{DS} is in-phase (red background region in Figure 4b);
4) $\Delta t_{peak} = T/2$ and $\Delta I_{peak} < 0$: the rGO-EGT exhibits half-wave rectification of the wave's negative half-cycle (light blue background in Figure 4b);
5) $\Delta t_{peak} = T/2$ and $\Delta I_{peak} > 0$: the rGO-EGT exhibits in-phase half-wave transduction of the wave's positive half-cycle (orange background in Figure 4b);
6) $\Delta t_{peak} = T/2$ and $\Delta I_{peak} = 0$: the rGO-EGT shows full-wave rectification of the input waveform. This happens under the specific condition of a waveform centered in a voltage window around the V_{CNP} of the rGO-EGT (Figure 4b, green dashed line).

Typical Δt_{peak} and ΔI_{peak} versus $V_{GS,Off}$ profiles are extracted for all the investigated f values and reported in Figure S6 (Supporting Information), showing a decrease in the width of the rectifying voltage window. This can be operationally defined as the V_{GS},*Off* range for which $\Delta t_{peak} = T/2$, and it progressively narrows as the frequency approaches 100 Hz. Here, Δt_{peak} equals T at all $V_{GS,Off}$ values, and, subsequently, the input signal is exclusively transduced. The dependency of the rectification voltage window width upon frequency is presented in Figure S7 (Supporting Information).

The influence of V_{pp} and f on the I_{DS} response was also investigated, in the condition of full-wave rectification, the results are depicted in Figure 4c,d, respectively.

In particular, Figure 4d depicts results for a set of experiments performed at constant $f = 1$ Hz while varying V_{pp} values. As seen, there is perfect rectification down to $V_{pp} = 0.025$ V, below which rectification does not occur. Figure 4d, concerning the response to sinusoidal waves of constant V_{pp} and different f values, shows the existence of a threshold frequency above which rectification does not occur anymore. The recorded I_{DS} for each frequency is normalized within the range of 0-1 it is plotted against the product of time and frequency, enabling direct comparison. At low frequency, I_{DS} shows two distinct rectified peaks up to the frequency of 100 Hz, where the two peaks start to collapse. At 500 Hz the signal is transduced perfectly out-of-phase, abiding the definition of displacement current in the electrolyte above the Maxwell-Wagner frequency.

3. Conclusion

This work presents how the ambipolar rGO-EGTs respond as filters to periodic input signals and as signal processing units. The range of frequencies subjected of filtering is tuned with the gate voltage, in good agreement with what was already observed with unipolar conductive polymers and organic semiconductors.[23,28] Besides this, when driven with gate voltage offset close to their charge neutrality point, rGO-EGTs exhibit both half-wave and full-wave rectification, showcasing good rectification capability in the range 1–100 Hz and with an input amplitude threshold of 25 mV, envisioning the possibility for real-time signal rectification in a single EGT. This signal processing paradigm, of utmost importance in electrophysiology, typically requires more complex circuitry, featuring at least two different EGTs, when using unipolar semi-conductive moieties.[40]

4. Experimental Section

Test Patterns: Devices are fabricated on quartz test patterns purchased from Fondazione Bruno Kessler (FBK, Trento, Italy), featuring gold interdigitated electrodes (geometric factor W/L = 500) patterned by photolithography and lift-off techniques. Pristine test patterns feature a protective photoresist layer over gold electrodes, which is removed by acetone rinsing. After photoresist layer removal, the test patterns are dried with nitrogen flux.

Device Fabrication: To fabricate rGO-EGTs, interdigitated electrodes are exposed to a commercial GO dispersion (0.4 wt.% in H_2O, monolayer content >95%, 2.2 < pH < 2.5, Graphenea Inc., US). rGO is potentiodynamically electrodeposited via cyclic voltammetry, short-circuiting the test pattern's gold electrodes (used as a single working electrode) to the "high-force" terminal of one of the two channels of a source/measure unit (SMU, Keysight B2912 A), closing the circuit by connecting a Pt-wire, bathing in the same GO dispersion, to the grounded "low-force" terminal (acting as a counter electrode).

Quasi-Static Electrical Characterization: The characterization layout is achieved using a 2-channel Keysight B2912A SMU, connecting the two interdigitated source and drain electrodes, bridged by the rGO film to the "low" and "high" terminals of channel 2, respectively. A Pt-wire connected at channel 1 "high" terminal is used as the Gate electrode. "Low" terminals of both channels are grounded. A phosphate buffer (1 M, pH = 7.4, P3619, Sigma–Aldrich) is used as the working electrolyte. Before the operation, devices are conditioned as described elsewhere.[44]

I–V transfer characteristics are acquired sweeping V_{GS} from −0.4 to 4 V (scan rate = 90 mV s^{-1}), while keeping V_{DS} equal to +0.3 V throughout the measurements.

I–V output characteristics are collected sweeping V_{DS} from −0.3 to +0.3 V, changing the V_{GS} value between the V_{DS} sweeps from −0.4 to 0.4 V with voltage steps of 0.1 V.

To extract the rGO-EGTs figure of merit, the devices' transfer characteristics are fit with the model presented by Zanotti et al., 2024. The transconductance profile has been numerically extracted as the first derivative of experimental data.[50]

Frequency-Dependent Electrical Characterization: An arbitrary waveform generator (Keysight EDU33212A) is used as a source of voltage sinusoidal signals at the gate. In particular, the input V_{GS} is a sinusoidal wave with a DC offset that varies linearly in time from −0.3 to 0.3 V. Both frequency (1, 2, 5, 10, 20, 50,100, 20 and 500 Hz) and peak-to-peak amplitude (0.2, 0.1, 0.064, 0.025 and 0.013 V) of input signals are systematically investigated, while drain-to-source voltage is kept fixed at 0.3 V.

In the assessment of filtering figures of merit, f_0 is determined as the frequency value at which γ is at its minimum, while cut-off frequencies (f_C, f_H, f_L) are determined as the frequency values at which γ is at 70% of its maximum value. The frequency dependency of γ is reproduced by a phenomenological fitting curve with the expression $\gamma = Af^B + Cf^D$.

Electrochemical Impedance Spectroscopy: A Gamry Reference 600 potentiostat/galvanostat is used to perform small-signal electrochemical impedance spectroscopy on the gate/electrolyte/channel/surface electrodes stack, for frequencies ranging from 1 Hz to 10 kHz, with a voltage amplitude of 10 mV. Measurements are performed in a two-electrode configuration, using the short-circuited source and drain terminals of the

rGO-EGT as the working electrode and connecting the Pt gate to the short-circuited counter and reference terminals of the potentiostat. In this configuration, application of a DC offset value at the working electrode – termed $V_{DC,WE}$ – enables to mimic the situation in which $V_{GS,Off} = - V_{DC,WE}$

Data Analysis: All the presented data have been analyzed using Matlab (version 9.10, Mathworks, Natick, MA, USA) and plotted using OriginPro2016. Figure panels have been assembled using Adobe Photoshop CS6, and 3D-device schematics are sketched in SketchUp Make 2017.

Supporting Information

Supporting Information is available from the Wiley Online Library or from the author.

Acknowledgements

This work had received funding from the European Union's Horizon Europe research and Innovation program under grant agreement No. 10109859, project Piezo4Spine, and by the Italian Ministry of Health under grant agreement PNRR-POC-2022-12376380, project BLBC. This work was conducted within the Technologies for Healthy Living Flagship and the Brain and Machines Flagship of the Istituto Italiano di Tecnologia.

Conflict of Interest

The authors declare no conflict of interest.

Data Availability Statement

The data that support the findings of this study are available from the corresponding author upon reasonable request.

Keywords

ambipolarity, EGOTs, organic electronics, organic transistors, rGO, signal processing

Received: July 4, 2025
Revised: September 25, 2025
Published online:

[1] E. Stein, O. Nahor, M. Stolov, V. Freger, I. M. Petruta, I. McCulloch, G. L. Frey, *Nat. Commun.* **2022**, *13*, 5548.
[2] M. T. Sharbati, Y. Du, J. Torres, N. D. Ardolino, M. Yun, F. Xiong, *Adv. Mater.* **2018**, *30*, 1.
[3] T. F. Schranghamer, A. Oberoi, S. Das, *Nat. Commun.* **2020**, *11*, 5474.
[4] M. Sensi, R. F. de Oliveira, M. Berto, M. Palmieri, E. Ruini, P. A. Livio, A. Conti, M. Pinti, C. Salvarani, A. Cossarizza, J. M. Cabot, J. Ricart, S. Casalini, M. B. González-García, P. Fanjul-Bolado, C. A. Bortolotti, P. Samorì, F. Biscarini, *Adv. Mater.* **2023**, *35*, 1.
[5] W. Fu, L. Feng, D. Mayer, G. Panaitov, D. Kireev, A. Offenhäusser, H. J. Krause, *Nano Lett.* **2016**, *16*, 2295.
[6] M. Ahsan, M. Akram, M. Iftikhar, T. U. Rehman, F. Garcia, A. Hasibuzzaman, F. A. Ozdemir, G. Sołowski, N. Fitria, *Journal of Medical research and Health Sciences* **2024**, *7*, 3157.
[7] N. Even-Chen, D. G. Muratore, S. D. Stavisky, L. R. Hochberg, J. M. Henderson, B. Murmann, K. V. Shenoy, *Nat. Biomed. Eng.* **2020**, *4*, 984.
[8] Y. Liu, A. Urso, R. Martins, T. Costa, V. Valente, V. Giagka, W. A. Serdijn, T. G. Constandinou, T. Denison, *IEEE Solid-State Circuits Magazine* **2020**, *12*, 30.
[9] U. Bruno, D. Rana, C. Ausilio, A. Mariano, O. Bettucci, S. Musall, C. Lubrano, F. Santoro, *Mater. Horiz.* **2024**, *11*, 2865.
[10] B. Alasingham, S. M. Ieee, *Precedeedings of the IEEE* **2019**, *107*, 1425.
[11] M. Berggren, A. Richter-Dahlfors, *Adv. Mater.* **2007**, *19*, 3201.
[12] M. Berto, C. Diacci, R. D'Agata, M. Pinti, E. Bianchini, M. Di Lauro, S. Casalini, A. Cossarizza, M. Berggren, D. Simon, G. Spoto, F. Biscarini, C. A. Bortolotti, *Adv. Biosyst.* **2018**, *2*, 1.
[13] F. Rondelli, M. Di Lauro, G. Calandra Sebastianaella, A. De Salvo, M. Genitoni, M. Murgia, P. Greco, C. G. Ferroni, R. Viaro, L. Fadiga, F. Biscarini, *Adv. Electron. Mater.* **2024**, *2400467*, 1.
[14] T. Yang, T. Shen, B. Duan, Z. Liu, C. Wang, *ACS Sens.* **2025**, *10*, 100.
[15] D. Khodagholy, T. Doublet, M. Gurfinkel, P. Quilichini, E. Ismailova, P. Leleux, T. Herve, S. Sanaur, C. Bernard, G. G. Malliaras, *Adv. Mater.* **2011**, *23*, H268.
[16] A. Campana, T. Cramer, D. T. Simon, M. Berggren, F. Biscarini, *Adv. Mater.* **2014**, *26*, 3874.
[17] M. Di Lauro, E. Zucchini, A. De Salvo, E. Delfino, M. Bianchi, M. Murgia, S. Carli, F. Biscarini, L. Fadiga, *Adv. Mater. Interfaces* **2022**, *9*, 2101798.
[18] M. Bianchi, A. De Salvo, M. Asplund, S. Carli, M. Di Lauro, A. Schulze-Bonhage, T. Stieglitz, L. Fadiga, F. Biscarini, M. Bianchi, A. De Salvo, S. Carli, M. Di Lauro, L. Fadiga, F. Biscarini, A. Schulze-Bonhage, T. Stieglitz, M. Asplund, **2021**.
[19] K. Feron, R. Lim, C. Sherwood, A. Keynes, A. Brichta, P. C. Dastoor, *Int. J. Mol. Sci.* **2018**, *19*, 2382.
[20] R. M. Owens, G. G. Malliaras, *MRS Bull.* **2012**, *35*, 86.
[21] J. Rivnay, R. M. Owens, G. G. Malliaras, *Chem. Mater.* **2014**, *26*, 679.
[22] B. D. Paulsen, K. Tybrandt, E. Stavrinidou, J. Rivnay, *Nat. Mater.* **2020**, *19*, 13.
[23] F. Rondelli, A. De Salvo, G. C. Sebastianella, M. Murgia, L. Fadiga, F. Biscarini, M. Di Lauro, *Neuromorphic Computing and Engineering* **2023**, *3*, 014004.
[24] H. Ling, D. A. Koutsouras, S. Kazemzadeh, Y. Van De Burgt, F. Yan, P. Gkoupidenis, *Appl. Phys. Rev.* **2020**, *7*, 011307.
[25] P. Gkoupidenis, N. Schaefer, B. Garlan, G. G. Malliaras, *Adv. Mater.* **2015**, *27*, 7176.
[26] I. Krauhausen, C. T. Coen, S. Spolaor, P. Gkoupidenis, Y. van de Burgt, *Adv. Funct. Mater.* **2024**, *34*, 2307729.
[27] M. J. Sultan, A. Bag, S. J. Hong, G. Wang, S. Kumar, H. H. Chouhdry, N. E. Lee, *Nano Energy* **2024**, *131*, 110202.
[28] A. De Salvo, F. Rondelli, M. Di Lauro, A. Tomassini, P. Greco, T. Stieglitz, L. Fadiga, F. Biscarini, *Adv. Mater. Interfaces* **2023**, *10*, 2300583.
[29] J. Zeng, X. Chen, S. Liu, Q. Chen, G. Liu, *Nanomaterials* **2023**, *13*, 803.
[30] M. Di Lauro, F. Rondelli, A. De Salvo, A. Corsini, M. Genitoni, P. Greco, M. Murgia, L. Fadiga, F. Biscarini, *Neuromorphic Computing and Engineering* **2024**, *4*, 024001.
[31] F. Torricelli, D. Z. Adrahtas, Z. Bao, M. Berggren, F. Biscarini, A. Bonfiglio, C. A. Bortolotti, C. D. Frisbie, E. Macchia, G. G. Malliaras, I. McCulloch, M. Moser, T.-Q. Nguyen, R. M. Owens, A. Salleo, A. Spanu, L. Torsi, *Nature Reviews Methods Primers* **2021**, *1*, 66.
[32] J. Rivnay, S. Inal, A. Salleo, R. M. Owens, M. Berggren, G. G. Malliaras, *Nat. Rev. Mater.* **2018**, *3*, 17086.
[33] R. A. Picca, K. Manoli, E. Macchia, L. Sarcina, C. Di Franco, N. Cioffi, D. Blasi, R. Österbacka, F. Torricelli, G. Scamarcio, L. Torsi, *Adv. Funct. Mater.* **2020**, *30*, 1.
[34] F. Vurro, E. Marchetti, M. Bettelli, L. Manfrini, A. Finco, C. Sportolaro, N. Coppedè, N. Palermo, M. G. Tommasini, A. Zappettini, M. Janni, *Chemosensors* **2023**, *11*, 374.
[35] J. Wang, L. Wang, J. Feng, C. Tang, X. Sun, H. Peng, *Adv. Fiber Mater.* **2021**, *3*, 47.

[36] M. Di Lauro, E. Zucchini, A. De Salvo, E. Delfino, M. Bianchi, M. Murgia, S. Carli, F. Biscarini, L. Fadiga, *Adv. Mater. Interfaces* **2022**, *9*, 2101798.
[37] D. Khodagholy, T. Doublet, P. Quilichini, M. Gurfinkel, P. Leleux, A. Ghestem, E. Ismailova, T. Hervé, S. Sanaur, C. Bernard, G. G. Malliaras, *Nat. Commun.* **2013**, *4*, 1575.
[38] S. T. Keene, C. Lubrano, S. Kazemzadeh, A. Melianas, Y. Tuchman, G. Polino, P. Scognamiglio, L. Cinà, A. Salleo, Y. van de Burgt, F. Santoro, *Nat. Mater.* **2020**, *19*, 969.
[39] G. M. Matrone, E. R. W. van Doremaele, A. Surendran, Z. Laswick, S. Griggs, G. Ye, I. McCulloch, F. Santoro, J. Rivnay, Y. van de Burgt, *Nat. Commun.* **2024**, *15*, 2868.
[40] C. Cea, G. D. Spyropoulos, P. Jastrzebska-Perfect, J. J. Ferrero, J. N. Gelinas, D. Khodagholy, *Nat. Mater.* **2020**, *19*, 679.
[41] Z. X. Wang, Z. Y. Zhang, L. M. Peng, *Chin. Sci. Bull.* **2012**, *57*, 2956.
[42] T. Q. Trung, N. T. Tien, D. Kim, M. Jang, O. J. Yoon, N. E. Lee, *Adv. Funct. Mater.* **2014**, *24*, 117.
[43] C. Reiner-Rozman, C. Kotlowski, W. Knoll, *Biosensors* **2016**, *6*, 17.
[44] M. Abouali, F. Rondelli, M. Genitoni, M. Murgia, M. Di Lauro, L. Fadiga, F. Biscarini, *Small* **2025**, *2502768*, 1.
[45] S. R. Laraba, W. Luo, A. Rezzoug, B. Wu, W. Chen, L. Xiao, Y. Yang, J. Wei, Y. Li, *Green Chem. Lett. Rev.* **2022**, *15*, 724.
[46] J. Chen, B. Yao, C. Li, G. Shi, *Carbon* **2013**, *64*, 225.
[47] F. Pasadas, A. Medina-Rull, F. G. Ruiz, J. N. Ramos-Silva, A. Pacheco-Sanchez, M. C. Pardo, A. Toral-Lopez, A. Godoy, E. Ramírez-García, D. Jiménez, E. G. Marin, *Small* **2023**, *19*, 1.
[48] Z. Wang, Z. Zhang, H. Zhong, T. Pei, S. Liang, L. Yang, S. Wang, L. M. Peng, *Adv. Funct. Mater.* **2013**, *23*, 446.
[49] G. Buzsáki, C. A. Anastassiou, C. Koch, *Nat. Rev. Neurosci.* **2012**, *13*, 407.
[50] R. Zanotti, M. Sensi, M. Berto, A. Paradisi, M. Bianchi, P. Greco, C. A. Bortolotti, M. Di Lauro, F. Biscarini, *Adv. Mater.* **2024**, *36*, 2410940.
[51] A. Svetlova, D. Kireev, G. Beltramo, D. Mayer, A. Offenhäusser, *ACS Appl. Electron. Mater.* **2021**, *3*, 5355.
[52] T. J. Neubert, M. Wehrhold, N. S. Kaya, K. Balasubramanian, *Nanotechnology* **2020**, *31*, 405201.
[53] T. J. Neubert, K. Balasubramanian, in *Graphene Field-Effect Transistors*, **2023**, pp. 231–250.
[54] Y. F. Chen, M. S. Fuhrer, *Phys. Rev. Lett.* **2005**, *95*, 1.
[55] I. Meric, M. Y. Han, A. F. Young, B. Ozyilmaz, P. Kim, K. L. Shepard, *Nat. Nanotechnol.* **2008**, *3*, 654.
[56] F. Schwierz, *Nat. Nanotechnol.* **2010**, *5*, 487.
[57] C. Tsonos, *Curr. Appl. Phys.* **2019**, *19*, 491.
[58] S. Drieschner, A. Guimerà, R. G. Cortadella, D. Viana, E. Makrygiannis, B. M. Blaschke, J. Vieten, J. A. Garrido, *Journal of Physics D:Applied Physics* **2017**, *50*, 095304.